ACS APPLIED MATERIALS & INTERFACES

Research Article

Cite This: ACS Appl. Mater. Interfaces 2018, 10, 15760−15766

www.acsami.org

New P2-Type Honeycomb-Layered Sodium-Ion Conductor: $Na_2Mg_2TeO_6$

HPSTAR 586-2018

Yuyu Li,[†] Zhi Deng,[†] Jian Peng,[†] Jintao Gu,[†] Enyi Chen,[†] Yao Yu,[†] Jianfang Wu,[†] Xiang Li,[†] Jiahuan Luo,[†] Yangyang Huang,[†] Yue Xu,[†] Zhonghui Gao,[‡] Chun Fang,[†] Jinlong Zhu,[§] Qing Li,[†] Jiantao Han,*[,†] and Yunhui Huang[†]

[†]State Key Laboratory of Material Processing and Die & Mould Technology, School of Materials Science and Engineering, Huazhong University of Science and Technology, Wuhan, Hubei 430074, China

[‡]School of Materials Science and Engineering, Tongji University, Shanghai 201804, China

[§]Center for High Pressure Science & Technology Advanced Research, Beijing 100094, China

Supporting Information

ABSTRACT: A novel solid sodium-ion conductor, $Na_2Mg_2TeO_6$ (NMTO) with a P2-type honeycomb-layered structure, has been synthesized for the first time by a simple solid-state synthetic route. The conductor of NMTO exhibits high conductivity of 2.3×10^{-4} S cm^{-1} at room temperature (RT) and a large electrochemical window of ~4.2 V (versus Na^+/Na). The conductor is remarkably stable, both in the ambient environment and within its metallic Na anode. This facile sodium-ion conductor displays potential for use in all-solid-state sodium-ion batteries (SS-SIBs).

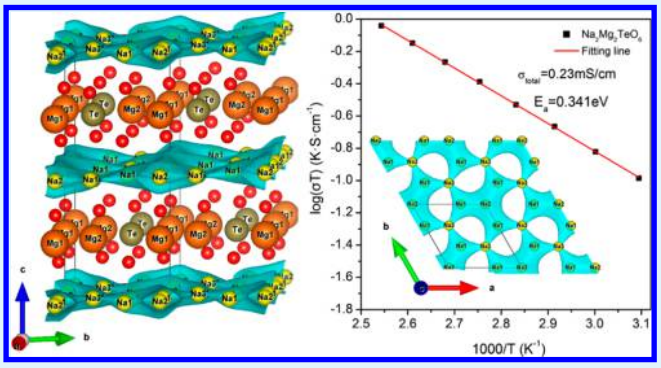

KEYWORDS: *$Na_2Mg_2TeO_6$, P2-type, layered, sodium-ion conductor, all-solid-state batteries*

INTRODUCTION

All-solid-state sodium-ion batteries (SS-SIBs) hold promise for large-scale energy storage systems because the batteries are affordable and relatively safe to use.[1−3] However, the lack of suitable solid-state electrolytes (SSEs) with high ionic conductivity, high chemical stability, and large electrochemical windows restricts the development of SS-SIBs.[4,5]

Unsuitable Electrolytes. Compared with solid polymer electrolytes (SPEs), inorganic solid electrolytes have high ionic conductivity, are nonflammable, and have large electrochemical windows.[6−8] Sulfide, selenide, borohydride, and oxide ceramic sodium conductors are common electrolytes for SSEs.[9−12] Sulfide, selenide, and borohydride electrolytes have higher ionic conductivity than that of oxide at room temperature (RT). However, they are unstable in air and harm the environment.[13−15]

Oxide electrolytes have attracted increasing attention because of their high ionic conductivity, large electrochemical windows, and high chemical stability.[16−18] β/β''-alumina and NASICON-type $Na_3Zr_2Si_2PO_{12}$ are two kinds of common oxide sodium solid electrolytes. Superionic conductor β/β''-alumina was commercialized early on and mainly applied in high-temperature Na−S batteries.[19,20] NASICON-type $Na_3Zr_2Si_2PO_{12}$ was discovered in 1976 by Hong et al., and its conductivity is ~1.0 $\times 10^{-3}$ S cm^{-1} at RT.[21] However, its stability is not suitable for sodium-ion systems because of poor electrolyte−electrode contact.[22]

Layered Oxides. Layered oxides have large Na^+ migration pathways between bonded 2D layers, thus showing high ionic conductivity at RT.[23−29] In 2011, a new family of layered sodium compound $Na_2M_2TeO_6$ (M = Ni, Co, Zn, Mg) was discovered, and the structures of $Na_2Ni_2TeO_6$ and $Na_2Zn_2TeO_6$ were revealed for the first time.[30]

In 2013, a heterovalent structure, $Na_2NiFeTeO_6$, was successfully synthesized by solid-state reaction, and its ionic conductivity is ~4×10^{-3} S cm^{-1} at 300 °C.[31] More recently, $Na_2Zn_2TeO_6$ (NZTO) and Ga-doped NZTO (NZTO-Gx) were reported with the high conductivity of 1.1×10^{-3} S cm^{-1} at RT, and they show excellent chemical stability. The high conductivity of NZTO-Gx is mainly attributed to adequate Na-site vacancies in the 2D network Na^+ diffusion layer.[32]

NMTO: A New Layered Oxide. With a similar crystal structure to NZTO,[30] $Na_2Mg_2TeO_6$ (NMTO) is a potential Na^+-ion conductor for SS-SIBs. In this work, and for the first time, NMTO was successfully synthesized by conventional solid-state reaction, and NMTO's crystal structure, spectra, ^{23}Na solid-NMR, and electrochemical performance were

Received: March 9, 2018
Accepted: April 24, 2018
Published: April 24, 2018

DOI: 10.1021/acsami.8b03938
ACS Appl. Mater. Interfaces 2018, 10, 15760−15766

investigated. NMTO shows high Na^+ conductivity of 2.3 × 10^{-4} S cm^{-1} at RT, along with a large electrochemical window of ~4.2 V (versus Na/Na^+), and high stability with metallic Na anodes.

RESULTS AND DISCUSSION

The XRD pattern and Rietveld refinement of NMTO are shown in Figure 1 and Table 1, respectively, without any

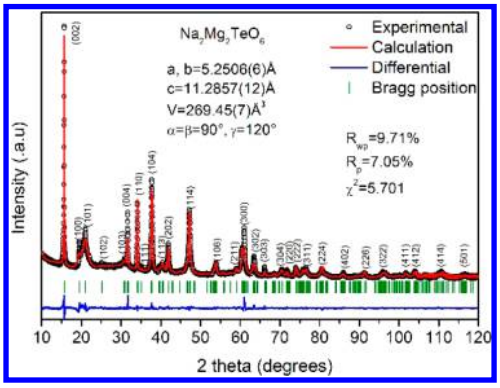

Figure 1. Rietveld refinement of the powder diffraction pattern for $Na_2Mg_2TeO_6$.

Table 1. X-ray Powder Diffraction Data for Na_2Mg_2TeO6 from Rietveld Refinement

compound	$Na_2Mg_2TeO_6$
space group	$P_{63}22$
$a = b$, c (Å)	5.251 (6), 11.286 (12)
$\alpha = \beta$, γ (deg)	90, 120
cell volume (Å^3)	269.45 (7)
number of formula units per unit cell Z	2
R_{wp} (%)	9.71
R_p (%)	7.05
$\chi 2$	5.701

impurity phase which appeared in Evstigneeva's.[30] The crystal parameters of NMTO are a = 5.2506 (6) Å and c = 11.2857 (12) Å, slightly smaller than those of NZTO (a = 5.2784 Å and c = 11.2895 Å)[32] because of the smaller diameter of Mg^{2+} (65 pm) than that of Zn^{2+} (74 pm). The superlattice reflections of NMTO are observed at l-odd-index peaks of (101) and (103), along with two weak l-even-index peaks of (100) and (102), fully resembling NZTO. The space group of NMTO is $P_{63}22$, and the columns are occupied solely by Mg atoms.[33] Figure 2a shows a white ceramic plate of NMTO with a diameter of 12.9 mm, and the relative density of NMTO is 87.2% measured by Archimedes principle. The morphologies of a cross-section of NMTO are displayed by scanning electron microscopy (SEM) in Figure 2b. The average size of particles that constitute NMTO ceramic is ~1 μm. Figure 2c shows the selected area electron diffraction (SAED) image of NMTO, and both of the crystal planes (103) and (222) can be indexed by the Bragg equation. Figure 2d shows that the lattice fringe of NMTO is a (002) crystal plane, according to the Bragg equation, with interplanar spacing of 5.5029 Å, which is smaller than that of NZTO (5.58 Å).

Figure 3 shows the crystal structure of NMTO and NZTO. Similar with NZTO's structure, the structure of NMTO can be indexed in a $P_{63}22$ space group, and its layered structure forms by $MgO_{6/3}$ and $TeO_{6/3}$ octahedra ordering in the plane along

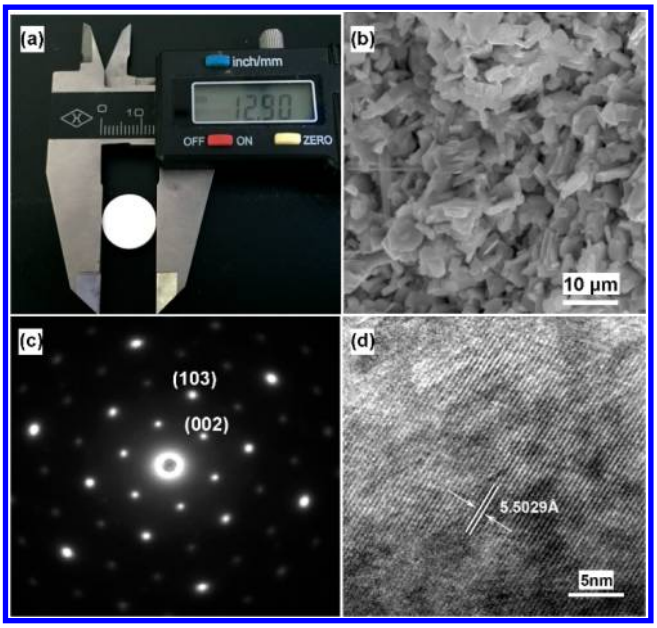

Figure 2. (a) Photo of $Na_2Mg_2TeO_6$ ceramic pellet. (b) SEM image of cross-sectional of $Na_2Mg_2TeO_6$. (c) Electron diffraction pattern of $Na_2Mg_2TeO_6$. (d) High-resolution TEM (HRTEM) image of $Na_2Mg_2TeO_6$.

shared edges, each $TeO_{6/3}$ octahedron being surrounded by six $MgO_{6/3}$. The result is a honeycomb structure within which Na^+ ions order in the plane between two layers. Mg atoms have two different sites in the crystal structure of NMTO, 2b (Mg1) and 2d (Mg2). Meanwhile, Na atoms have three sites, 6g (Na1), 2a (Na2), and 4f (Na3). Na1 is located in the middle of two tetrahedral holes that are formed by two $MgO_{6/3}$ and one $TeO_{6/3}$ octahedra; Na2 is sandwiched between the triangular faces of $MgO_{6/3}$ octahedra, and Na3 is between $MgO_{6/3}$ octahedra and $TeO_{6/3}$ octahedra. Therefore, NMTO has a typical P2-type honeycomb layering. The bond lengths of Na−O of NMTO and NZTO are shown in the bottom of Figure 3 and listed in Table 2, respectively. The Na−O bonds of NMTO are smaller than those of NZTO, indicating larger acting force during the process of Na^+ migration in the lattice of NMTO than that of NZTO. Figure 4 shows the 3D bond valence difference map isosurfaces of NMTO from the a axis (Figure 4a) and c axis (Figure 4b) calculated by bond valence sum (BVS), illustrating that Na^+ in NMTO can transfer freely in three Na sites, similar to NZTO and different form Na_xCoO_2[34] and $Na_2Ni_2TeO_6$.[35] The migration barrier of Na^+ transport in the interlayer of NMTO is 2.55 eV, larger than of NZTO, 2.1 eV, indicating that the migration of Na^+ in NMTO is more difficult than in NZTO.

Table 3 shows the Wyckoff positions, atomic coordinates, U_{iso}, and occupancies of NMTO from Rietveld refinements. All Na sites are partially vacant [Na (1), occ 0.52; Na (2), occ 0.07; Na (3), occ 0.41; occ, occupancy], providing all-important crossover points that enable the fast ion conduction that we observe by experiment (see below). Interestingly, the average Na−Na distance of NMTO is 3.07 Å, larger than that of NZTO (2.54 Å)[30] (see Table 4), which suggests that NMTO has a smaller electron−electron Coulomb interaction. The thermogravimetric analysis (TGA) and differential scanning calorimetry (DSC) show a very stable heating process from RT to 500 °C, except a less than 1% weight loss and a small endothermic process observed at 100 °C (see Figure S1), which is related to

DOI: 10.1021/acsami.8b03938
ACS Appl. Mater. Interfaces 2018, 10, 15760−15766

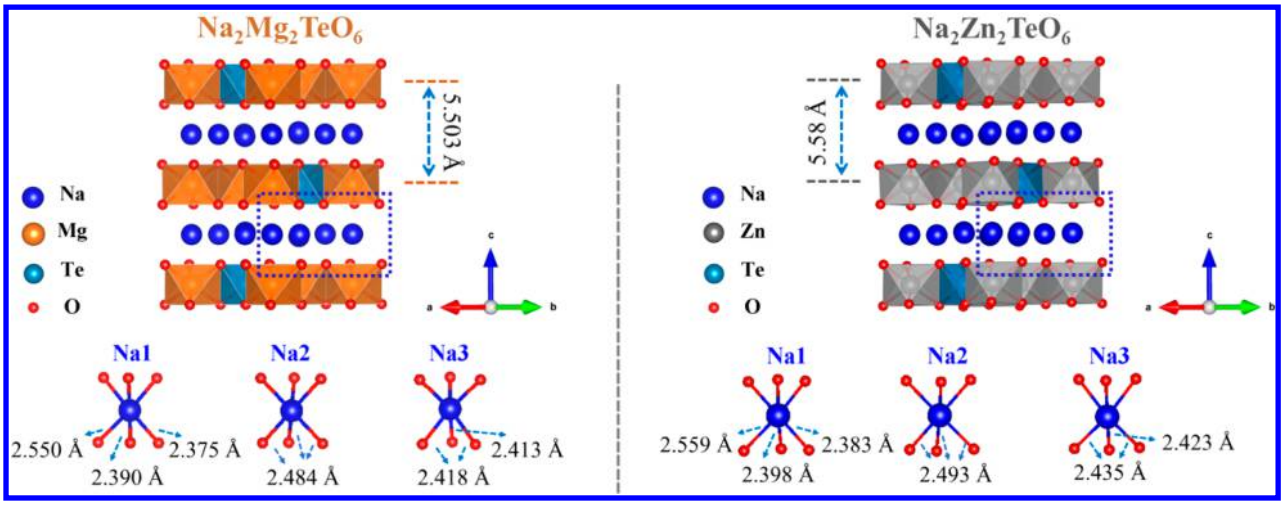

Figure 3. Crystal structure and Na−O bond length of $Na_2Mg_2TeO_6$ (left) and $Na_2Zn_2TeO_6$ (right) viewed from (110).

Table 2. Principal Interatomic Distances (Å) in $Na_2Mg_2TeO_6$ and $Na_2Zn_2TeO_6$

type	$Na_2Mg_2TeO_6$	$Na_2Zn_2TeO_6$
Te−O	1.964 (15) × 6	1.971 (6) × 6
M1−O (M = Mg, Zn)	2.139 (17) × 6	2.148 (5) × 6
M2−O (M = Mg, Zn)	2.153 (17) × 6	2.162 (6) × 6
Na1−O	2.550 (19) × 2	2.559 (6) × 2
	2.391 (18) × 2	2.398 (6) × 2
	2.375 (17) × 2	2.383 (8) × 2
average	2.439	2.45
Na2−O	2.485 (18) × 6	2.493 (5) × 6
Na3−O	2.413 (18) × 3	2.422 (9) × 3
	2.418 (18) × 3	2.435 (10) × 3
average	2.415	2.429

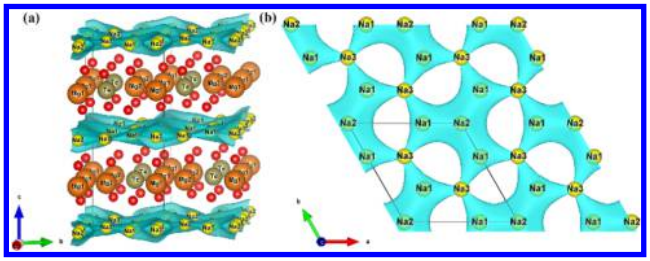

Figure 4. Three-dimensional bond valence difference map isosurfaces for $Na_2Mg_2TeO_6$ with isosurfaces of (a) *a* axis, (b) *c* axis v. u. for Na ions.

Table 3. Wyckoff Positions, Atomic Coordinates, U_{iso}, and Occupancies of $Na_2Mg_2TeO_6$ from Rietveld Refinement

type	Wyckoff	atomic coordinate			U_{iso}	occupancy
Te	2c	0.33	0.67	0.25	0.007	1
Mg1	2b	0	0	0.25	0.001	1
Mg2	2d	0.33	0.67	0.75	0.001	1
Na1	6g	0.66	0	0	0.009	0.52
Na2	2i	0	0	0	0.452	0.67
Na3	4f	0.33	0.67	0.51	0.003	0.41
O	12i	0.36	0.33	0.65	0.011	1

a little water absorption and hygroscopy on particle surfaces. In addition, upon comparison with fresh as-prepared samples, the lattice parameters of a 1 month stored sample have no

Table 4. Na−Na Distances (Å) in $Na_2Mg_2TeO_6$

compound	$Na_2Mg_2TeO_6$
Na1−Na1	3.00820 (32) × 4
	3.07840 (32) × 2
Na1−Na2	3.4733 (4) × 3
	1.77732 (19) × 3
average	2.62531
Na1−Na3	5.5160 (4) × 3
	1.74129 (18) × 3
average	3.62865
Na2−Na3	3.030416 (32) × 6
Na3−Na3	3.04190 (32) × 6
average	3.07121

significant change (see Figure S2), which reveals that NMTO is highly stable in the ambient environment.

Figure 5a shows the electrochemical impedance spectroscopy (EIS) spectra of NMTO at RT with a typical semicircle at high

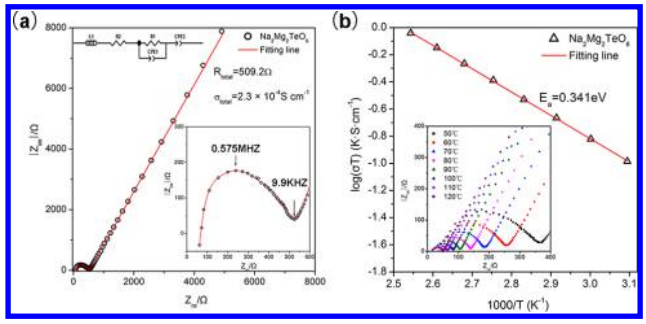

Figure 5. (a) EIS of $Na_2Mg_2TeO_6$ at room temperature. (b) Arrhenius conductivity plot of $Na_2Mg_2TeO_6$ from 50 to 120 °C. Inset: Nyquist impedance plots of $Na_2Mg_2TeO_6$ from 50 to 120 °C.

frequency and one Warburg-type region at low frequency. The total resistance of NMTO ceramic is 509.2 Ω, and the total conductivity of NMTO is 2.3×10^{-4} S cm^{-1}, which is obtained by Ohm's law. From the composition of total resistance of NMTO, the bulk resistance is 95.7 Ω, lesser than grain-boundary resistance 413.5 Ω, which illustrated that NMTO has high grain-boundary resistance. Figure S3 shows the DC-polarization properties of NMTO at RT. The stabilized current that represents NMTO's electronic motion is much smaller

DOI: 10.1021/acsami.8b03938
ACS Appl. Mater. Interfaces 2018, 10, 15760−15766

than the initial current that represents all charge carriers' motions. The result illustrates that the electronic conductivity is much lower than the ionic one in NMTO, confirming that NMTO is a typical ionic conductor.

Figure 5b shows the reciprocal temperature dependence of the total ionic conductivity of NMTO. The linear dependence of log σ versus $(1/T)$ follows the Arrhenius law: $\sigma_t = A \exp(-E_a/k_B T)$, where σ_t is the total conductivity, A is the pre-exponential parameter, T is absolute temperature, and k_B is the Boltzmann constant. The inset in Figure 5b shows the representative Nyquist plots of NMTO at the temperature range 50−120 °C. The shapes of these spectra are characteristic of ionic conductors, and the total resistance is reduced with increased temperature. As a result, E_a of NMTO is 0.341 eV, smaller than that of NASICON, ∼0.385 eV. The main reasons are large interlayers and abundant Na^+ vacancies in NMTO. The larger interlayers induce longer Na−O bonds and decrease Coulomb force between Na^+ and O^{2-}, while abundant Na^+ vacancies not only increase the concentration of current carriers but also decrease Na^+ migration energy (E_m). However, E_a of NMTO is larger than that of NZTO (0.327 eV),[32] which confirmed with the result of the BVS calculation, because of the smaller interlayer d-spacing increasing the attractive force between Na^+ and O^{2-}, resulting in the migration energy of Na^+ in NMTO being higher than in NZTO.

Figure 6a shows ^{23}Na NMR spin−lattice relaxation rates T_1^{-1} versus inverse temperature of NMTO. For NMTO, T_1^{-1}

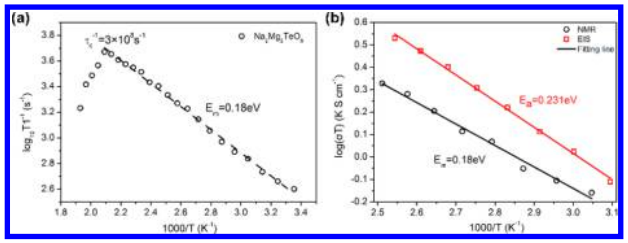

Figure 6. (a) ^{23}Na NMR spin−lattice relaxation rates T_1^{-1} versus inverse temperature for $Na_2Mg_2TeO_6$. (b) Activation energy calculated by EIS from bulk Na-ion conductivity of $Na_2Mg_2TeO_6$ compared with migration energy calculated by ^{23}Na NMR T_1^{-1} measurements.

increases linearly to a maximum and then drops off with increasing temperature. At the maximum, the condition $\omega_0\tau \approx 1$ is fulfilled with the motional correlation time (i.e., the Na^+ hopping time τ) being ideal for the frequency distribution to be effective for relaxation. In Figure 4a, as $\omega_0/2\pi$ = 105.8 MHz, the Na^+ hopping rate $\tau_0^{-1} \approx 6.6 \times 10^8$ s^{-1} of NMTO can be reached at 200 °C. The migration energy of NMTO is 0.18 eV, which is calculated by the slope of spin−lattice relaxation rates T_1^{-1} versus inverse temperature between RT to 200 °C, and is greater than that of NZTO, which is caused by NMTO having smaller interlayer spacing than NZTO, comporting with the result of active energy measurement. ^{23}Na NMR results show that the diffusion coefficient of NMTO is 3.19×10^{-12} at 55 °C, and the ionic conductivity σ_{NMR} is 2.11×10^{-3} S cm^{-1}, smaller than that of NZTO, and comporting with the results of EIS measurement. Figure 6b compares bulk activation energy E_a calculated by bulk resistance of EIS and migration energy E_m calculated by results of NMR in NMTO. The results of E_a and E_m of NMTO are significantly close, 0.231 and 0.18 eV, and confirm each other, which verifies that the result of NMR is dependable.

Figure 7a shows the electrochemical window of NMTO with metallic Na investigated by cyclic voltammetry (CV) measure-

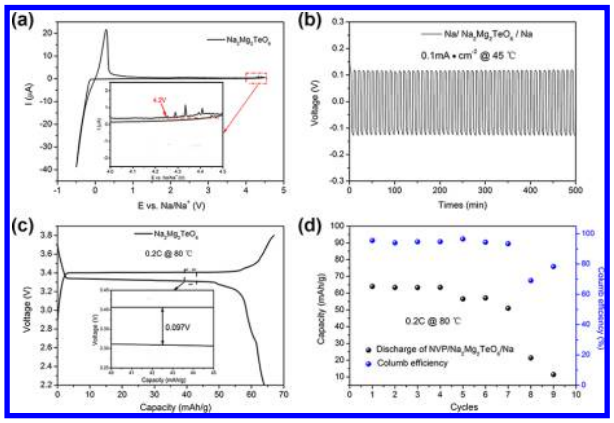

Figure 7. (a) Cyclic voltammogram in a symmetric steel/$Na_2Mg_2TeO_6$/Na cell from −0.5 to 4.5 V at scanning rate of 5 mV s^{-1}. (b) Cyclability of $Na_2Mg_2TeO_6$ in a symmetric Na/$Na_2Mg_2TeO_6$/Na cell with a current density of 0.1 mA cm^2 at 45 °C. (c) Charge and discharge curve of the second cycle of NVP/$Na_2Mg_2TeO_6$/Na under 0.2 C at 80 °C. The inset displays the polarization of the battery. (d) Cycle performance of NVP/$Na_2Mg_2TeO_6$/Na under 0.2 C at 80 °C.

ments in Na/NMTO/steel cells. An obvious anodic peak, larger than that of NZTO, appears at close to 4.2 V, which suggests that NMTO is electrochemically stable with metallic Na with an electrochemical window of 4.2 V (versus Na^+/Na), without adverse side reactions. Figure 7b shows the electrochemical stability of NMTO with metallic Na illustrated by galvanostatic cycling of a symmetric Na/NMTO/Na cell with a current density of 0.1 mA cm^{-2} at 45 °C. The results demonstrate that sodium is plated and stripped fully reversibly with a low overpotential reaching a maximum of ∼100 mV for 50 cycles, and the calculated resistance of the interface between NMTO and metallic Na is ∼420 Ω. The stable voltage fluctuation demonstrates that NMTO has excellent stability with metallic Na. Figure 7c shows the charge and discharge curves of SS-SIBs built with $Na_3V_2(PO_4)_3$ cathodes that use NMTO solid electrolyte and metallic Na anodes with a current rate of 0.2 C at 80 °C. The SS-SIBs with NMTO electrolyte display a small polarization of 0.091 V and reversible capacity of ∼65 mA h g^{-1} in the first cycle, less than the capacity of 100 mA h g^{-1} in practical charge−discharge performance (as shown in Figure S4). The reason for this phenomenon could be related to a consumption of Na in NVP in the interface between NVP cathode and NMTO solid electrolyte.[36] Figure 7d shows the cycle performance at 80 °C of the NVP/NMTO/Na all-solid-state battery. It exhibits stable cycle performance before 8 cycles at 80 °C. However, at 45 °C and room temperature (Figure S5), the capacity of the NVP/NMTO/Na all-solid-state battery is close to 0 in every cycle. The poor performance at 45 °C and room temperature is due to high interface resistance of the NVP/NMTO/Na all-solid-state battery. This problem can be improved by surface treatment of electrode and electrolyte in the next work. For example, introducing a "buffer layer", such as Si coating on the garnet electrolyte, could enable a conformal interface to reduce the resistance of the interface between electrode and electrolyte,[37] demonstrating that a 3D bilayer electrolyte could provide a high loading of cathode and more continuous ion pathway between cathode and electrolyte to reduce the resistance of the interface between cathode and

DOI: 10.1021/acsami.8b03938
ACS Appl. Mater. Interfaces 2018, 10, 15760−15766

electrolyte.[38] Despite all of this, these performances demonstrate that NMTO is a promising electrolyte for fabricating advanced SS-SIBs.

CONCLUSION

In conclusion, we report a novel NMTO sodium-ion conductor as a solid electrolyte for SS-SIBs. Combining XRD, ^{23}Na NMR, and EIS analyses shows that this solid electrolyte has a P2-type layered structure with a $P_{63}22$ space group, and the Na^+ migration pathway in the crystal lattice is in the interlayers between two honeycomb frameworks of NMTO and has been simulated by BVS. NMTO exhibits high ionic conductivity of 2.3×10^{-4} S cm^{-1} at RT that only requires a simple solid-state synthetic route. It also shows excellent chemical stability under ambient conditions, a large electrochemical window of ~4.2 V (versus Na^+/Na), and high stability with metallic Na. The all-solid-state battery NVP/NMTO/Na works properly with a current rate of 0.2 C at 80 °C. These results will lead to a progressive development of SS-SIBs.

EXPERIMENTAL SECTION

Solid Electrolyte Synthesis. Polycrystalline $Na_2Mg_2TeO_6$ (NMTO) was prepared by conventional solid-state reaction. Sodium carbonates (Na_2CO_3, Aldrich, 99.9%), magnesium oxide (MgO, Aladdin, 99.9%), and tellurium oxide (TeO_2, Aladdin, 99.9%) were mixed with the stoichiometric proportion; the powders were ball-milled for 30 min and calcined in air at 700 °C for 12 h with heating rate of 2 °C min^{-1}. After regrinding and pressing, the powders were cold-pressed into pellets at 100 MPa and then sintered at 850 °C for 6 h with a heating rate of 2 °C min^{-1}. To avoid the contamination of Al^{3+}, the pristine powder was placed between the crucible and the pellet during sintering.

$Na_3V_2(PO_4)_3$ Cathode Synthesis. The $Na_3V_2(PO_4)_3$ cathode was synthesized by a conventional solid-state reaction. Stoichiometric starting materials Na_2CO_3, V_2O_5, and $NH_3H_2PO_4$ were thoroughly mixed, ground in a mortar using ethanol as a reagent. Subsequently, the pellets were heated at 350 °C for 6 h and 800 °C for 10 h in Ar/H_2 and cooled down to room temperature naturally. All chemicals were used directly without any further purification and were analytical reagents.

Structural and Thermostability Characterization. Thermogravimetric analysis (TGA) of the NMTO samples was performed using a PerkinElmer diamond TG apparatus carried out from 25 to 500 °C under an N_2 flow (20 mL min^{-1}) with a heating rate of 5 °C min^{-1}. DSC profiles were recorded on a PerkinElmer DSC8000 instrument under a N_2 flow (20 mL min^{-1}) with a scan rate of 10 °C min^{-1} from 25 to 500 °C. X-ray diffraction (XRD) patterns of the samples were collected using an X'pert Pro powder diffractometer (PANalytical) with Cu Kα radiation in the range 2θ = 10−80°. Rietveld refinements were performed using GSAS software with the EXPGUI interface to determine the crystallographic data.[39] The morphology and microstructure of the prepared materials were characterized by scanning electron microscopy (FE-SEM, JEOL).

Electrochemical Characterization. Electrochemical impedance spectroscopy (EIS) measurements were conducted using a Princeton P4000 frequency response analyzer between 1 MHz and 1 Hz at the amplitude of 100 mV. Pellets (12 mm diameter and ~3 mm in thickness) for the EIS measurement were sparked Au as the blocking electrode. For the Arrhenius plot, the temperature was raised from 50 to 120 °C in a drying oven (Jin Hong).

The electronic conductivity of the NMTO solid electrolytes was evaluated by the DC-polarization measurement, with the cold-pressed pellet (12 mm diameter and ~3 mm in thickness) with Au as the blocking electrode for the DC-polarization measurement, using a Princeton 4000 instrument with a constant voltage (1 V). The voltage was held for 40 min, and the electronic conductivity was calculated from the stabilized current and constant voltage by Ohm's law.

NMTO pellets (12 mm diameter and ~3 mm in thickness) for cyclic voltammetry studies were sparked Au on one side to be a blocking electrode, and Na foils were carefully attached on the other side. Cyclic voltammetry investigations were conducted using a Princeton 4000 instrument with a scan rate of 5 mV s^{-1} between −0.5 and 4.5 V versus Na^+/Na at 45 °C. NMTO pellets (12 mm diameter and ~3 mm in thickness) for symmetric cells and cyclic voltammetry studies were attached to Na foil on two sides. Then, the assembled symmetric cells were cycled with a current density of 0.1 mA cm^{-2} at room temperature.

^{23}Na Solid-NMR Spectroscopy. ^{23}Na NMR experiments were conducted at the Larmor frequency of 105.8 MHz using a Bruker Avance III 400 spectrometer with a 0.7 cm high-temperature MAS probe and spin rate of 3000 Hz. The saturation-recovery method was applied to measure the spin−lattice relaxation rate (T_1^{-1}) with the 90° pulse length of 4.5 μs. For NMTO, measurements were carried out at the temperature ranging from 25 to 225 °C. The temperature was calibrated with $Pb(NO_3)_2$, and chemical shift of ^{23}Na was referenced to 1 mol L^{-1} NaCl aqueous solution.

Characterization of All-Solid-State Batteries. The fabrication of all-solid-state sodium-ion batteries was carried out in an Ar-filled glovebox. One electrode was fabricated by mixing $Na_3V_2(PO4)_3$ (NVP) powder, Ketjen black, poly (vinylidene fluoride) (PVDF), and $Na(CF_3SO_2)_2N$ (NaTFSI) in an agate mortar with a mass ratio of 4:1:1:4. The mixture was dispersed in *N*-methyl-2-pyrrolidone (NMP) and coated on one side of NMTO pellets. Then, the solid electrolyte with electrode coating was dried in a vacuum oven at 80 °C for 12 h to remove NMP and trace moisture. The loading mass of the electrode was ~1 mg. Afterward, sodium metal was attached on the other side of the NMTO pellet. Finally, a laminated SS-SIB was assembled into a 2032-coin cell, and the charge/discharge tests were performed on a battery testing system (Neware Electronics, China) at room temperature between 2.0 and 3.8 V versus Na/Na^+.

ASSOCIATED CONTENT

Supporting Information

The Supporting Information is available free of charge on the ACS Publications website at DOI: 10.1021/acsami.8b03938.

TG and DSC curves, Rietveld refinement of the XRD, DC-polarization curve, and cycle performance (PDF)

AUTHOR INFORMATION

Corresponding Author

*E-mail: jthan@hust.edu.cn.

ORCID

Jiahuan Luo: 0000-0003-3194-6520

Qing Li: 0000-0003-4807-030X

Jiantao Han: 0000-0002-1302-7136

Notes

The authors declare no competing financial interest.

ACKNOWLEDGMENTS

This work was supported by the Natural Science Foundation of China (Grant 2016YFB010030X, 2016YFB0700600) and the National Natural Science Foundation of China (Grants 51772117 and 51732005). The authors also thank the Analytical and Testing Centre of HUST and the State Key Laboratory of Materials Processing and Die & Mold Technology of HUST for XRD, SEM, TEM, TGA, and other measurements.

REFERENCES

(1) Armand, M.; Tarascon, J. M. Building better batteries. *Nature* **2008**, *451* (7179), 652−657.

(2) Luo, J.; Sun, S.; Peng, J.; Liu, B.; Huang, Y.; Wang, K.; Zhang, Q.; Li, Y.; Jin, Y.; Liu, Y.; Qiu, Y.; Li, L.; Han, J.; Huang, Y. Graphene-Roll-Wrapped Prussian Blue Nanospheres as a High-Performance Binder-Free Cathode for Sodium-Ion Batteries. *ACS Appl. Mater. Interfaces* **2017**, *9* (30), 25317−25322.
(3) Xu, G.-L.; Amine, R.; Xu, Y.-F.; Liu, J.; Gim, J.; Ma, T.; Ren, Y.; Sun, C.; Liu, Y.; Zhang, X.; Heald, S. M.; Solhy, A.; Saadoune, I.; Mattis, W. L.; Sun, S.-G.; Chen, Z.; Amine, K. Insights into the Structural Effects of Layered Cathode Materials for High Voltage Sodium-ion Batteries. *Energy Environ. Sci.* **2017**, *10* (7), 1677−1693.
(4) Hansen, B. R. S.; Paskevicius, M.; Jorgensen, M.; Jensen, T. R. Halogenated Sodium-closo-Dodecaboranes as Solid-State Ion Conductors. *Chem. Mater.* **2017**, *29* (8), 3423−3430.
(5) Nguyen, H.; Hy, S.; Wu, E.; Deng, Z.; Samiee, M.; Yersak, T.; Luo, J.; Ong, S. P.; Meng, Y. S. Experimental and Computational Evaluation of a Sodium-Rich Anti-Perovskite for Solid State Electrolytes. *J. Electrochem. Soc.* **2016**, *163* (10), A2165−A2171.
(6) Wu, J. F.; Chen, E. Y.; Yu, Y.; Liu, L.; Wu, Y.; Pang, W. K.; Peterson, V. K.; Guo, X. Gallium-Doped $Li_7La_3Zr_2O_{12}$ Garnet-Type Electrolytes with High Lithium-Ion Conductivity. *ACS Appl. Mater. Interfaces* **2017**, *9* (2), 1542−1552.
(7) Pecher, O.; Carretero-González, J.; Griffith, K. J.; Grey, C. P. Materials' Methods: NMR in Battery Research. *Chem. Mater.* **2017**, *29* (1), 213−242.
(8) Kamaya, N.; Homma, K.; Yamakawa, Y.; Hirayama, M.; Kanno, R.; Yonemura, M.; Kamiyama, T.; Kato, Y.; Hama, S.; Kawamoto, K.; Mitsui, A. A lithium superionic conductor. *Nat. Mater.* **2011**, *10* (9), 682−686.
(9) Kato, Y.; Hori, S.; Saito, T.; Suzuki, K.; Hirayama, M.; Mitsui, A.; Yonemura, M.; Iba, H.; Kanno, R. High-power all-solid-state batteries using sulfide superionic conductors. *Nature Energy* **2016**, *1* (4), 16030.
(10) Zhang, L.; Yang, K.; Mi, J.; Lu, L.; Zhao, L.; Wang, L.; Li, Y.; Zeng, H. Na_3PSe_4: A Novel Chalcogenide Solid Electrolyte with High Ionic Conductivity. *Adv. Energy Mater.* **2015**, *5* (24), 1501294.
(11) Duchêne, L.; Kühnel, R.-S.; Stilp, E.; Cuervo-Reyes, E.; Remhof, A.; Hagemann, H.; Battaglia, C. A stable 3 V all-solid-state sodium-ion battery based on a closo-borate electrolyte. *Energy Environ. Sci.* **2017**, *10*, 2609−2615.
(12) Park, H.; Jung, K.; Nezafati, M.; Kim, C. S.; Kang, B. Sodium Ion Diffusion in Nasicon ($Na_3Zr_2Si_2PO_{12}$) Solid Electrolytes: Effects of Excess Sodium. *ACS Appl. Mater. Interfaces* **2016**, *8* (41), 27814−27824.
(13) Richards, W. D.; Miara, L. J.; Wang, Y.; Kim, J. C.; Ceder, G. Interface Stability in Solid-State Batteries. *Chem. Mater.* **2016**, *28* (1), 266−273.
(14) Yu, Z.; Shang, S. L.; Seo, J. H.; Wang, D.; Luo, X.; Huang, Q.; Chen, S.; Lu, J.; Li, X.; Liu, Z. K.; Wang, D. Exceptionally High Ionic Conductivity in $Na_3P_{0.62}As_{0.38}S_4$ with Improved Moisture Stability for Solid-State Sodium-Ion Batteries. *Adv. Mater.* **2017**, *29* (16), 1605561.
(15) Yan, Y.; Kuhnel, R.-S.; Remhof, A.; Duchene, L.; Reyes, E. C.; Rentsch, D.; Lodziana, Z.; Battaglia, C. A Lithium Amide-Borohydride Solid-State Electrolyte with Lithium-Ion Conductivities Comparable to Liquid Electrolytes. *Adv. Energy Mater.* **2017**, *7* (19), 1700294.
(16) Francisco, B. E.; Stoldt, C. R.; M'Peko, J.-C. Lithium-Ion Trapping from Local Structural Distortions in Sodium Super Ionic Conductor (NASICON) Electrolytes. *Chem. Mater.* **2014**, *26* (16), 4741−4749.
(17) Han, X. G.; Gong, Y. H.; Fu, K.; He, X. F.; Hitz, G. T.; Dai, J. Q.; Pearse, A.; Liu, B. Y.; Wang, H.; Rublo, G.; Mo, Y. F.; Thangadurai, V.; Wachsman, E. D.; Hu, L. B. Negating interfacial impedance in garnet-based solid-state Li metal batteries. *Nat. Mater.* **2016**, *16* (5), 572−579.
(18) Xu, H.; Wang, S.; Wilson, H.; Zhao, F.; Manthiram, A. Y-Doped NASICON-type $LiZr_2(PO_4)_3$ Solid Electrolytes for Lithium-Metal Batteries. *Chem. Mater.* **2017**, *29* (17), 7206−7212.
(19) Lu, X.; Xia, G.; Lemmon, J. P.; Yang, Z. Advanced materials for sodium-beta alumina batteries: Status, challenges and perspectives. *J. Power Sources* **2010**, *195* (9), 2431−2442.
(20) Lee, D.-H.; Lee, S.-T.; Kim, J.-S.; Lim, S.-K. Analysis of properties of partially stabilized zirconia-doped Na^+-beta-alumina prepared by calcining-cum-sintering process. *Mater. Res. Bull.* **2017**, *96*, 143−148.
(21) Hong, H. Y. P. Crystal structures and crystal chemistry in the system $Na_{1+x}Zr_2Si_xP_{3-x}O_{12}$. *Mater. Res. Bull.* **1976**, *11* (2), 173−182.
(22) Zhang, Z.; Zhang, Q.; Shi, J.; Chu, Y. S.; Yu, X.; Xu, K.; Ge, M.; Yan, H.; Li, W.; Gu, L.; Hu, Y.-S.; Li, H.; Yang, X.-Q.; Chen, L.; Huang, X. A Self-Forming Composite Electrolyte for Solid-State Sodium Battery with Ultralong Cycle Life. *Adv. Energy Mater.* **2017**, *7* (4), 1601196.
(23) Gupta, A.; Mullins, C. B.; Goodenough, J. B. $Na_2Ni_2TeO_6$: Evaluation as a cathode for sodium battery. *J. Power Sources* **2013**, *243*, 817−821.
(24) Smaha, R. W.; Roudebush, J. H.; Herb, J. T.; Seibel, E. M.; Krizan, J. W.; Fox, G. M.; Huang, Q.; Arnold, C. B.; Cava, R. J. Tuning Sodium Ion Conductivity in the Layered Honeycomb Oxide $Na_{3-x}Sn_{2-x}Sb_xNaO_6$. *Inorg. Chem.* **2015**, *54* (16), 7985−7991.
(25) Wang, P.-F.; Guo, Y.-J.; Duan, H.; Zuo, T.-T.; Hu, E.; Attenkofer, K.; Li, H.; Zhao, X. S.; Yin, Y.-X.; Yu, X.; Guo, Y.-G. Honeycomb-Ordered $Na_3Ni_{1.5}M_{0.5}BiO_6$ (M = Ni, Cu, Mg, Zn) as High-Voltage Layered Cathodes for Sodium-Ion Batteries. *ACS Energy Letters* **2017**, *2* (12), 2715−2722.
(26) Wang, P.-F.; Yao, H.-R.; You, Y.; Sun, Y.-G.; Yin, Y.-X.; Guo, Y.-G. Understanding the structural evolution and Na^+ kinetics in honeycomb-ordered O3-$Na_3Ni_2SbO_6$ cathodes. *Nano Res.* **2017**, DOI: 10.1007/s12274-017-1863-1.
(27) Wang, P.-F.; You, Y.; Yin, Y.-X.; Guo, Y.-G. Layered Oxide Cathodes for Sodium-Ion Batteries: Phase Transition, Air Stability, and Performance. *Adv. Energy Mater.* **2018**, *8* (8), 1701912.
(28) You, Y.; Kim, S. O.; Manthiram, A. A Honeycomb-Layered Oxide Cathode for Sodium-Ion Batteries with Suppressed P3-O1 Phase Transition. *Adv. Energy Mater.* **2017**, *7* (5), 1601698.
(29) You, Y.; Manthiram, A. Progress in High-Voltage Cathode Materials for Rechargeable Sodium-Ion Batteries. *Adv. Energy Mater.* **2018**, *8* (2), 1701785.
(30) Evstigneeva, M. A.; Nalbandyan, V. B.; Petrenko, A. A.; Medvedev, B. S.; Kataev, A. A. A New Family of Fast Sodium Ion Conductors: $Na_2M_2TeO_6$(M = Ni, Co, Zn, Mg). *Chem. Mater.* **2011**, *23* (5), 1174−1181.
(31) Nalbandyan, V. B.; Petrenko, A. A.; Evstigneeva, M. A. Heterovalent substitutions in $Na_2M_2TeO_6$ family: Crystal structure, fast sodium ion conduction and phase transition of $Na_2LiFeTeO_6$. *Solid State Ionics* **2013**, *233*, 7−11.
(32) Li, Y.; Deng, Z.; Peng, J.; Chen, E.; Yu, Y.; Li, X.; Luo, J.; Huang, Y.; Zhu, J.; Fang, C.; Li, Q.; Han, J.; Huang, Y. A P2-type layered superionic conductor Ga-doped $Na_2Zn_2TeO_6$ for all-solid-state sodium-ion batteries. *Chem. - Eur. J.* **2018**, *24* (5), 1057−1061.
(33) Berthelot, R.; Schmidt, W.; Sleight, A. W.; Subramanian, M. A. Studies on solid solutions based on layered honeycomb-ordered phases P2-$Na_2M_2TeO_6$ (M = Co, Ni, Zn). *J. Solid State Chem.* **2012**, *196*, 225−231.
(34) Mo, Y.; Ong, S. P.; Ceder, G. Insights into Diffusion Mechanisms in P2 Layered Oxide Materials by First-Principles Calculations. *Chem. Mater.* **2014**, *26* (18), 5208−5214.
(35) Sau, K.; Kumar, P. P. Ion Transport in $Na_2M_2TeO_6$: Insights from Molecular Dynamics Simulation. *J. Phys. Chem. C* **2015**, *119* (4), 1651−1658.
(36) Yu, X. W.; Manthiram, A. Electrode-Electrolyte Interfaces in Lithium-Sulfur Batteries with Liquid or Inorganic Solid Electrolytes. *Acc. Chem. Res.* **2017**, *50* (11), 2653−2660.
(37) Luo, W.; Gong, Y.; Zhu, Y.; Fu, K. K.; Dai, J.; Lacey, S. D.; Wang, C.; Liu, B.; Han, X.; Mo, Y.; Wachsman, E. D.; Hu, L. Transition from Superlithiophobicity to Superlithiophilicity of Garnet Solid-State Electrolyte. *J. Am. Chem. Soc.* **2016**, *138* (37), 12258−12262.
(38) Fu, K.; Gong, Y.; Hitz, G. T.; McOwen, D. W.; Li, Y.; Xu, S.; Wen, Y.; Zhang, L.; Wang, C.; Pastel, G.; Dai, J.; Liu, B.; Xie, H.; Yao, Y.; Wachsman, E. D.; Hu, L. Three-dimensional bilayer garnet solid

DOI: 10.1021/acsami.8b03938
ACS Appl. Mater. Interfaces 2018, 10, 15760−15766

electrolyte based high energy density lithium metal-sulfur batteries. *Energy Environ. Sci.* **2017**, *10* (7), 1568−1575.
(39) Toby, B. H. EXPGUI, a graphical user interface for GSAS. *J. Appl. Crystallogr.* **2001**, *34*, 210−213.

DOI: 10.1021/acsami.8b03938
ACS Appl. Mater. Interfaces 2018, 10, 15760−15766